Volume 26
Number 18
14 May 2024
Pages 13517–14090

PCCP

Physical Chemistry Chemical Physics

rsc.li/pccp

25 YEARS ANNIVERSARY

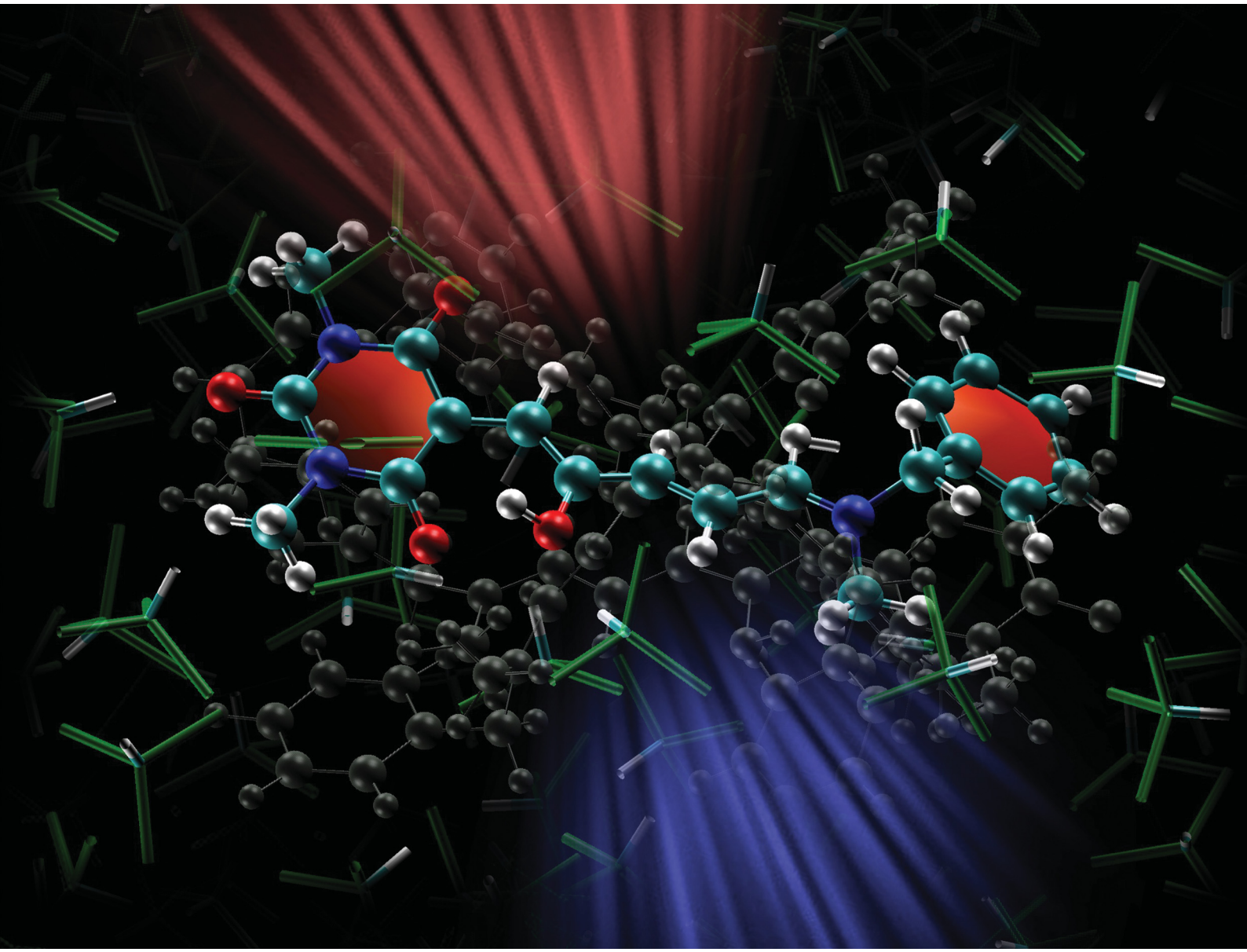

ISSN 1463-9076

ROYAL SOCIETY OF CHEMISTRY

PAPER

Angela Dellai, Giacomo Prampolini, Frédéric Castet *et al.* Dynamic effects on the nonlinear optical properties of donor acceptor stenhouse adducts: insights from combined MD + QM simulations

PCCP Owner Societies

PCCP

PAPER

View Article Online
View Journal | View Issue

Cite this: *Phys. Chem. Chem. Phys.*, 2024, **26**, 13639

Dynamic effects on the nonlinear optical properties of donor acceptor stenhouse adducts: insights from combined MD + QM simulations†

Angela Dellai, *[a] Carmelo Naim, [ab] Javier Cerezo, [c] Giacomo Prampolini *[d] and Frédéric Castet *[a]

The second-order nonlinear optical (NLO) responses of a donor–acceptor stenhouse adduct (DASA) are investigated by using a computational approach combining molecular dynamics simulations and density functional theory (DFT) calculations. Specific force fields for the open and closed photoswitching forms are first parameterized and validated according to the Joyce protocol, in order to finely reproduce the geometrical features and potential energy surfaces of both isomers in chloroform solution. Then, DFT calculations are performed on structural snapshots extracted at regular time steps of the MD trajectories to address the influence of the thermalized conformational dynamics on the NLO responses related to hyper-Rayleigh scattering (HRS) experiments. We show that accounting for the structural dynamics largely enhances the HRS hyperpolarizability (β_{HRS}) compared to DFT calculations considering solely equilibrium geometries, and greatly improves the agreement with experimental measurements. Furthermore, we show that the NLO responses of the NLO-active open form are correlated with the bond order alternation along the triene bridge connecting the donor and acceptor moieties, which is rationalized using simple essential state models.

Received 23rd January 2024,
Accepted 5th March 2024

DOI: 10.1039/d4cp00310a

rsc.li/pccp

1 Introduction

Stenhouse donor–acceptor adducts (DASAs) are a class of organic molecules first synthesized by Read De Alanis and colleagues in 2014,[1,2] that have attracted much interest over the past decade due to unique reverse photochromic properties. The structure of these systems comprises an amine donor and a dicarboxylate acceptor from either Meldrums or barbituric acids at the terminal positions of a π-conjugated triene bridge. When exposed to visible light, DASAs photoisomerize from the thermodynamically stable conjugated (open) form to a non-conjugated cyclic (closed) form, undergoing a loss of color that reversibly recovers in the dark. The design of successive generations of DASAs upon variation of the substitution pattern, rationalized by quantum chemistry calculations, further demonstrated high tunability in their photoswitching behavior and excellent fatigue resistance.[3–16] In addition, the significant change in (photo)physical and chemical properties upon photoisomerization makes DASAs very useful for many applications, ranging from colorimetric sensing to photo-induced drug-delivery systems.[17,18] Recently, the potential of DASAs for exploitation within light-responsive nonlinear optical (NLO) materials and devices has also been demonstrated. Quantum-chemical calculations performed on a large number of DASA derivatives predicted that the alteration of the π-electron conjugation along the photocommutation should induce a significant contrast in the first hyperpolarizability (β),[19,20] which was subsequently proved experimentally by means of hyper-Rayleigh scattering (HRS) measurements.[21] These extensive experimental and theoretical investigations allowed to identify the BA4 derivative (Fig. 1), incorporating a barbituric acid (BA) acceptor moiety and a tertiary amine donor, as a highly effective NLO switch due to its fast and efficient photoconversion, intermediate time constant for the back reaction, and high contrast in the second-harmonic (SH) intensity.

In this theoretical contribution, we investigate further the second-order NLO responses of BA4 in both its closed and open forms, by taking into account the effects of thermally-induced

[a] *Univ. Bordeaux, CNRS, Bordeaux INP, Institut des Sciences Moléculaires, UMR 5255, F-33400 Talence, France. E-mail: angela.dellai@u-bordeaux.fr, frederic.castet@u-bordeaux.fr*
[b] *Donostia International Physics Center (DIPC), Manuel Lardizabal Ibilbidea 4, 20018 Donostia, Euskadi, Spain*
[c] *Departamento de Química and Institute for Advanced Research in Chemical Sciences (IAdChem), Universidad Autónoma de Madrid, 28049 Madrid, Spain*
[d] *Consiglio Nazionale delle Ricerche, CNR-ICCOM, Pisa, Italy. E-mail: giacomo.prampolini@pi.iccom.cnr.it*

† Electronic supplementary information (ESI) available: QMD-FF parameters; Complementary data on geometrical and electronic parameters and on optical properties; details on the calculation of the β_{zxx}/β_{zzz} ratio. See DOI: https://doi.org/10.1039/d4cp00310a

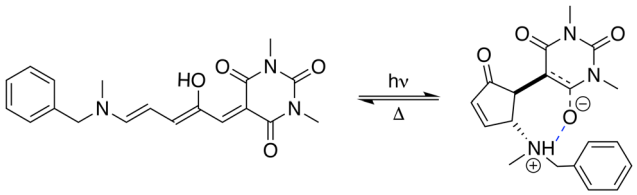

Fig. 1 Photocommutation between the open and zwitterionic closed forms of BA4.

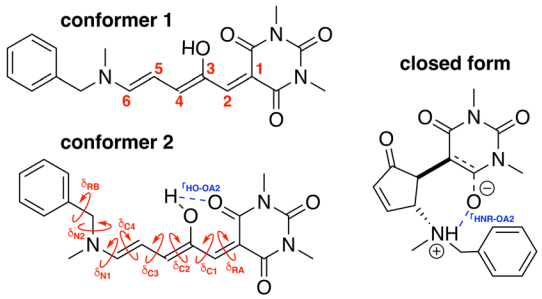

Fig. 2 Possible open conformers (left) and zwitterionic closed form (right) of BA4. Torsional angles and intramolecular non-bonded interactions discussed in the text are also displayed.

fluctuations in the geometry of the chromophore. Indeed, molecular hyperpolarizabilities are highly sensitive to geometrical distortions, and structural dynamic effects have been shown to play a leading role in the NLO properties of organic dyes.[22] The computational approach involves classical molecular dynamics (MD) simulations and subsequent quantum chemistry (QM) calculations performed at the density functional theory (DFT) level on statistical samplings of uncorrelated molecular snapshots extracted from the MD trajectories. This sequential MD + QM (or MD + DFT) scheme[23–26] has been previously employed to characterize the SH responses of various organic species in solution, including photochromic compounds.[27–35] For example, it was shown to drastically improve the description of the first hyperpolarizability contrast between the open and closed forms of switchable indolinooxazolidine derivatives.[28]

However, this computational strategy requires the development of highly accurate and system-specific force fields (FFs), as the NLO properties targeted by DFT calculations have high sensitivity to geometrical changes. Therefore, the first part of this work was dedicated to the derivation of force-fields able to precisely reproduce the structural features of BA4 in both its open and closed forms. Concretely, two quantum mechanically derived force-fields (QMD-FFs[36–38]) were specifically tailored for either the open or closed BA4 forms, based on QM descriptors purposely computed at the DFT level. In the second part, the second-order NLO responses of BA4 and their variation upon switching were computed at the DFT level along the MD trajectories obtained with the QMD-FFs and validated against previously reported experimental data.[21] The influence of dynamic geometrical distortions was then analyzed in detail and rationalized in the light of simple essential state models.

2 Theory and methods

2.1 Training molecular descriptors

To build the training database required by the QMD-FF parameterization, selected molecular descriptors were computed at QM (DFT) level for both the open and closed form of BA4. In fact, as previously reported,[21,39] DASA derivatives incorporating non-symmetric amines can adopt two different conformations in their open form (Fig. 2), the first one with the smaller substituent in the upper position being slightly more stable (with a Gibbs free energy difference of 0.45 kcal mol^{-1} at 298 K). Moreover, the most stable closed form of BA4 in chloroform adopts a zwitterionic structure, as illustrated in Fig. 2. Following the standard Joyce procedure,[36,37] the QM training data set for each form is composed by the optimized geometry, its Hessian matrix and relaxed torsional energy scans along the most flexible coordinates. To this end, reference geometries for both forms of BA4 were obtained by optimizing all coordinates using DFT, and the Hessian matrices were computed at these conformations. In addition, the relaxed energy profiles were obtained by minimizing all internal coordinates but the scanned dihedral. All DFT calculations were performed using the Gaussian16 package,[40] employing the M06-2X[41] exchange–correlation functional (XCF) with the aug-cc-pVDZ basis set, accounting for dispersion effects by means of the Grimme's D3 correction[42] and for solvent effects (here chloroform) by using the solvation model based on density (SMD),[43] which was shown to reproduce the relative thermal stability of open and closed DASA isomers more accurately than other polarizable continuum models.[21] At this level of approximation, selected according to benchmark calculations reported in ref. 21, the open-to-closed Gibbs isomerization energy is equal to 6.73 kcal mol^{-1}.

2.2 QMD-FF parameterization

Based on the aforementioned QM training molecular descriptors, two separate QMD-FFs, for either BA4 open and closed forms, were parameterized exploiting the standard partition[38,44–46] of the total QMD-FF energy, $E^{\text{total}}_{\text{QMD-FF}}$, in an intramolecular contribution, ruling the molecular flexibility and an intermolecular term, which describes the interaction with the solvent:

$$E^{\text{total}}_{\text{QMD-FF}} = E^{\text{intra}}_{\text{QMD-FF}} + E^{\text{inter}}_{\text{QMD-FF}} \quad (1)$$

The interactions between the BA4 solute and the surrounding chloroform molecules, is hence accounted as:

$$E^{\text{inter}}_{\text{QMD-FF}} = \sum_{i=1}^{N_{\text{BA4}}} \sum_{j=1}^{5} E_{ij}^{\text{BA4-CHCl}_3} \quad (2)$$

where i and j run on the atoms of the N_{BA4} solute and $CHCl_3$ solvent, respectively, whereas $E_{ij}^{\text{BA4-CHCl}_3}$ takes the standard expression:

$$E_{ij} = \left(4\epsilon_{ij}^{\text{inter}}\left[\left(\frac{\sigma_{ij}^{\text{inter}}}{r_{ij}}\right)^{12} - \left(\frac{\sigma_{ij}^{\text{inter}}}{r_{ij}}\right)^{6}\right]\right) + \left(\frac{q_i q_j}{4\pi\epsilon_0 r_{ij}}\right) \quad (3)$$

The first term in square brackets on the right side of eqn (3) is the standard 12–6 Lennard-Jones (LJ) potential, while the second term accounts for the Coulomb charge–charge interactions. In the present work, only the latter term was derived from QM data, whereas the LJ intermolecular parameters, consistently with the description chosen for the $CHCl_3$ solvent, were transferred from the OPLS database.[47,48] Conversely, the point charges were specifically derived through the RESP method from the DFT electronic density of either the open or closed isomers, exploiting their optimized geometries computed for the Joyce parameterization. A full list of the intermolecular parameters for both forms is reported in the ESI† (Tables S1 and S7).

The QMD-FF parameterization of the intramolecular term in eqn (1) was carried out according to the Joyce protocol,[36,37] thus computing $E^{\text{intra}}_{\text{QMD-FF}}$ as:

$$E^{\text{intra}}_{\text{QMD-FF}} = \sum_{i}^{N_{\text{str}}} E_{\text{s}}(r_i) + \sum_{i}^{N_{\text{bnd}}} E_{\text{b}}(\theta_i) + \sum_{i}^{N_{\text{stors}}} E_{\text{st}}(\phi_i) + \sum_{i}^{N_{\text{ftors}}} E_{\text{ft}}(\delta_i) + E^{\text{LJ}}_{\text{Nb}} \quad (4)$$

where the first two terms describe stretching and bending contributions, respectively:

$$E_{\text{s}}(r_i) = \frac{1}{2}k^{\text{s}}_i\left(r_i - r^0_i\right)^2;\; E_{\text{b}}(\theta_i) = \frac{1}{2}k^{\text{b}}_i\left(\theta_i - \theta^0_i\right)^2 \quad (5)$$

being $k^{\text{s}}(k^{\text{b}})$ and $r^0(\theta^0)$ the harmonic force constants and equilibrium values. According to the standard Joyce procedure,[26,36,46,49] the same harmonic expression is employed to describe dihedrals, ϕ, which are expected to be subjected to small oscillations around their equilibrium position, as those ruling the planarity of stiff aromatic rings or double bonds, *i.e.*:

$$\Delta E_{\text{st}}(\phi_i) = \frac{1}{2}k^{\text{st}}_i\left(\phi_i - \phi^0_i\right)^2 \quad (6)$$

where k^{st}_i and ϕ^0_i are the force constant and equilibrium angle for the stiff torsion i. Conversely, the more flexible dihedrals δ are described through sums of Fourier-like terms:

$$\Delta E_{\text{ft}}(\delta_i) = \sum_{k}^{N^{\cos}_i} c_{ik}[1 + \cos(n_{ik}\delta_{ik} + \gamma_{ik})] \quad (7)$$

Finally, as the MD runs are expected to explore a large portion of the potential energy surface (PES) of the target molecule, in which the open form might be found in varied conformations, intramolecular non-bonded interactions were introduced between selected atom pairs, to account for both the steric repulsion between close atoms and the possible intramolecular hydrogen bonds (HBs). Following the Joyce protocol, such interactions can be introduced through specific LJ intramolecular model functions as:

$$\Delta E^{\text{LJ}}_{\text{nb}}(r_{ij}) = 4\epsilon^{\text{intra}}_{ij}\left[\left(\frac{\sigma^{\text{intra}}_{ij}}{r_{ij}}\right)^{12} - \left(\frac{\sigma^{\text{intra}}_{ij}}{r_{ij}}\right)^{6}\right] \quad (8)$$

It is worth noticing that ϵ^{intra} and σ^{intra}, the intramolecular LJ parameters entering in the above equation and describing the interaction between selected atom pairs belonging to the same molecule (BA4), differ from ϵ and σ reported in (3), which were instead designed to mimic the interaction among atoms pertaining to two different molecules (here BA4 and chlorofrom).

Once all potential terms have been assigned to each coordinate, the QMD-FF parameters (*i.e.* all equilibrium coordinates and force constants) were simultaneously determined from the stored QM molecular descriptors with the Joyce software,[50] by minimizing the standard[36,37] objective function:

$$I^{\text{intra}} = \sum_{K\le L}^{3N-6}\frac{2W''_{KL}}{C}\left[H_{KL} - \left(\frac{\partial^2 E^{\text{intra}}_{\text{QMD-FF}}}{\partial Q_K \partial Q_L}\right)\right]^2_{g_0} + \sum_{g}^{N_{\text{geom}}} W_g\left[\Delta U - E^{\text{intra}}_{\text{QMD-FF}}\right]^2_g \quad (9)$$

where the sum in the first term runs over the $3N - 6$ dye's normal modes ($\boldsymbol{Q}$), C is a normalization factor, and H_{KL} an element of the QM Hessian matrix, evaluated in the minimum energy geometry (g_0). In the second term, ΔU_g is the QM computed energy difference between the g and g_0 geometries, while N_{geom} is the number of different geometrical arrangements sampled along the QM relaxed energy scans. The weights W''_{KL} and W_g were set, as in most recent applications,[37,38,46,49,51,52] to 2500 (for $K \neq L$), 5000 (for the diagonal elements) and 1.0 for all g geometries.

2.3 Molecular dynamics

MD simulations were carried out with the Gromacs code[53] employing the parameterized QMD-FFs, either on each isolated (gas phase) DASA isomer or on a system consisting of one open or closed isomer and ~1000 explicit chloroform molecules. Simulations were performed in the NVT ensemble at 298 K for the isolated molecule in the gas phase and at constant pressure and temperature (NPT, 1 atm and 298 K) in solution. For the isolated molecule, a 5 ns trajectory at 298 K was produced, storing DASA's conformations every 100 ps. Conversely, the solvated system was equilibrated in the NPT ensemble for 5 ns, keeping temperature (298 K) and pressure (1 atm) constant in the NPT ensemble through the Berendsen algorithm.[54] Thereafter, a 10 ns production run was carried out, keeping the same temperature and pressure constant through the Bussi–Parrinello[55] and Parrinello–Rahman[56] schemes, which are capable to preserve the correct statistics in the NPT ensemble. In all runs, unless otherwise stated, no bond length was constrained and the time step was set to 0.25 fs. A cut-off distance of 12 Å was employed for short-range interactions, and the standard correction for energy and virial applied to LJ potentials. Long range electrostatic was accounted for by the particle mesh Ewald scheme (PME). Temperature and pressure coupling constants τ_T and τ_P were set to 0.1 ps and 5 ps, respectively.

2.4 Reference molecular properties

The parameterized QMD-FFs were validated by comparing geometrical, electronic and optical properties calculated using

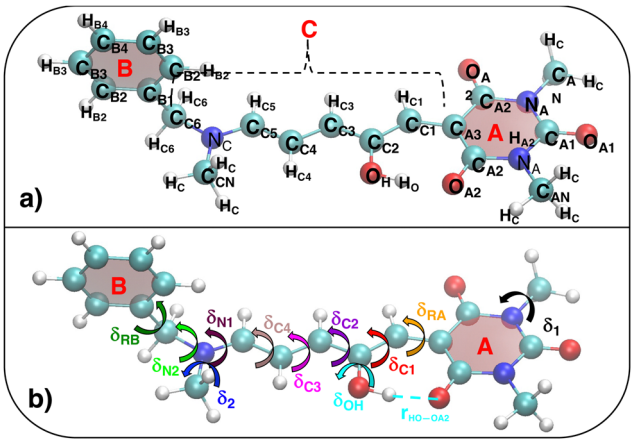

Fig. 3 (a) Specific atom labeling adopted during the Joyce parameterization for the open DASA isomer. Only symmetry- or chemically equivalent atoms share the same label. All label suffixes refer to the fragmentation scheme evidenced with the red letters: A (ring A), B (ring B) and C (Chain). (b) Definition and labeling of the most flexible dihedrals of the open DASA isomer, all handled by the QMD-FF through eqn (7), unless otherwise stated. The internal non-bonded coordinate $r_{H_O\cdots O_{A2}}$ (see eqn (8)) is also evidenced with a dashed cyan line.

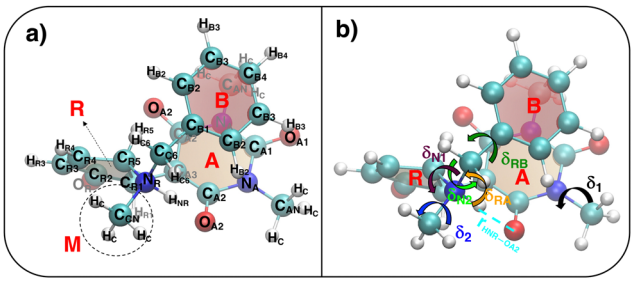

Fig. 4 (a) Specific atom labeling adopted during the Joyce parameterization for the closed DASA isomer. Only symmetry- or chemically equivalent atoms share the same label. All label suffixes refer to the fragmentation scheme evidenced with the red letters: A (ring A), B (ring B) and R (ring C) and M (methyl). (b) Definition and labeling of the most flexible dihedrals of the closed DASA isomer, all handled by the QMD-FF through eqn (7). The internal non-bonded coordinate $r_{H_{NR}\cdots O_{A2}}$ (eqn (8)), is also evidenced with a dashed cyan line.

MD geometries with those obtained from reference DFT calculations. Concerning the structural descriptors, particular attention was paid to the torsional degrees of freedom defined by the dihedral angles (δ) shown in Fig. 2 (see Fig. 3 and 4 for 3D representations), and to the length of intramolecular HBs ($r_{H_O\text{–}O_{A2}}$ and $r_{H_{NR}\text{–}O_{A2}}$).

For the conjugated open form, the planarity of the central part is measured through the dihedral angle ξ = 1-2-5-6 (see Fig. 2 for atom labels), while the overall molecular length is estimated through the OA1–NC distance (see Fig. 3). Additionally, bond length alternation (BLA) and bond order alternation (BOA) along the triene bridge are defined as:

$$\mathrm{BLA} = \frac{d_{23} + d_{45}}{2} - \frac{d_{12} + d_{34} + d_{56}}{3} \tag{10}$$

$$\mathrm{BOA} = \frac{o_{23} + o_{45}}{2} - \frac{o_{12} + o_{34} + o_{56}}{3} \tag{11}$$

where d_{ij} and o_{ij} are bond distances and bond orders between atoms i and j, respectively. The bond order o_{ij} estimates the number of electrons fluctuating concurrently between atoms i and j. The different atoms are defined according to the quantum theory of atoms in molecules (QTAIM)[57] and their corresponding overlap integrals were obtained from the AIMAll software.[58] Finally, the bond orders were calculated using the ESI-3D code[59–61] using the following expression:[62,63]

$$o_{ij} = 2\int_i\int_j \rho_{xc}(\mathbf{r}_1, \mathbf{r}_2)\mathrm{d}\mathbf{r}_1\mathrm{d}\mathbf{r}_2 = -2\mathrm{cov}(N_i, N_j) \tag{12}$$

where N_i and N_j are the atomic populations and $\rho_{xc}(\mathbf{r}_1, \mathbf{r}_2)$ is the exchange–correlation density. Note that, while π-conjugation metrics like BLA and BOA are known to be highly sensitive to the choice of XCF,[64–66] the M06-2X XCF was shown to reliably describe these indicators for extended π-conjugated systems.[67,68]

Turning to the optical properties, the Franck–Condon vertical absorption energies between the ground and first excited states, as well as the second-order NLO responses, were calculated using time-dependent (TD) DFT at the SMD:M06-2X/6-311+G(d) level. More specifically, the investigated NLO responses are related to hyper-Rayleigh scattering (HRS) experiments, in which the intensity of the light at the second harmonic frequency, collected perpendicularly to the incident laser beam, is proportional to the square of the first hyperpolarizability of the molecular scatterers. Assuming a vertical polarization of the scattered light (parallel to the Z axis of the laboratory frame) and a non-polarized incident light (*i.e.* including both vertical and horizontal components along Z and X, respectively), the HRS hyperpolarizability reads:

$$\begin{aligned}\beta_{\mathrm{HRS}}(-2\omega;\omega,\omega) &= \sqrt{\langle\beta_{ZZZ}{}^2\rangle + \langle\beta_{ZXX}{}^2\rangle} \\ &= \sqrt{\langle\beta_{ZZZ}{}^2\rangle(1 + 1/\mathrm{DR})}\end{aligned} \tag{13}$$

where the $\langle\beta_{ZZZ}{}^2\rangle$ and $\langle\beta_{ZXX}{}^2\rangle$ rotational averages can be written in terms of molecular β tensor components as follows:

$$\begin{aligned}\langle\beta_{ZZZ}{}^2\rangle = {} & \frac{1}{7}\sum_{\zeta}^{x,y,z}\beta_{\zeta\zeta\zeta}{}^2 + \frac{4}{35}\sum_{\zeta\neq\eta}^{x,y,z}\beta_{\zeta\zeta\eta}{}^2 + \frac{2}{35}\sum_{\zeta\neq\eta}^{x,y,z}\beta_{\zeta\zeta\zeta}\beta_{\zeta\eta\eta} \\ & + \frac{4}{35}\sum_{\zeta\neq\eta}^{x,y,z}\beta_{\eta\zeta\zeta}\beta_{\zeta\zeta\eta} + \frac{4}{35}\sum_{\zeta\neq\eta}^{x,y,z}\beta_{\zeta\zeta\zeta}\beta_{\eta\eta\zeta} + \frac{1}{35}\sum_{\zeta\neq\eta}^{x,y,z}\beta_{\eta\zeta\zeta}{}^2 \\ & + \frac{4}{105}\sum_{\zeta\neq\eta\neq\xi}^{x,y,z}\beta_{\zeta\zeta\eta}\beta_{\eta\xi\xi} + \frac{1}{105}\sum_{\zeta\neq\eta\neq\xi}^{x,y,z}\beta_{\eta\zeta\zeta}\beta_{\eta\xi\xi} \\ & + \frac{4}{105}\sum_{\zeta\neq\eta\neq\xi}^{x,y,z}\beta_{\zeta\zeta\eta}\beta_{\xi\xi\eta} \\ & + \frac{2}{105}\sum_{\zeta\neq\eta\neq\xi}^{x,y,z}\beta_{\zeta\eta\xi}{}^2 + \frac{4}{105}\sum_{\zeta\neq\eta\neq\xi}^{x,y,z}\beta_{\zeta\eta\xi}\beta_{\eta\zeta\xi}\end{aligned} \tag{14}$$

$$\langle \beta_{ZXX}{}^2 \rangle = \frac{1}{35}\sum_{\zeta}^{x,y,z}\beta_{\zeta\zeta\zeta}{}^2 + \frac{4}{105}\sum_{\zeta\neq\eta}^{x,y,z}\beta_{\zeta\zeta\zeta}\beta_{\zeta\eta\eta} - \frac{2}{35}\sum_{\zeta\neq\eta}^{x,y,z}\beta_{\zeta\zeta\zeta}\beta_{\eta\eta\zeta} + \frac{8}{105}\sum_{\zeta\neq\eta}^{x,y,z}\beta_{\zeta\zeta\eta}{}^2 + \frac{3}{35}\sum_{\zeta\neq\eta}^{x,y,z}\beta_{\zeta\eta\eta}{}^2 - \frac{2}{35}\sum_{\zeta\neq\eta}^{x,y,z}\beta_{\zeta\zeta\eta}\beta_{\eta\zeta\zeta} + \frac{1}{35}\sum_{\zeta\neq\eta\neq\xi}^{x,y,z}\beta_{\zeta\eta\eta}\beta_{\zeta\xi\xi} - \frac{2}{105}\sum_{\zeta\neq\eta\neq\xi}^{x,y,z}\beta_{\zeta\zeta\xi}\beta_{\eta\eta\xi} - \frac{2}{105}\sum_{\zeta\neq\eta\neq\xi}^{x,y,z}\beta_{\zeta\zeta\eta}\beta_{\eta\xi\xi} + \frac{2}{35}\sum_{\zeta\neq\eta\neq\xi}^{x,y,z}\beta_{\zeta\eta\xi}{}^2 - \frac{2}{105}\sum_{\zeta\neq\eta\neq\xi}^{x,y,z}\beta_{\zeta\eta\xi}\beta_{\eta\zeta\xi} \quad (15)$$

The depolarization ratio (DR in eqn (13)) is defined as the ratio between these two components and provides information on the symmetry of the second harmonic scatterer. It ranges from 3/2 for pure octupolar compounds to 9 for pure dipolar ones. For strong push–pull π-conjugated molecules, the hyperpolarizability tensor is largely dominated by the diagonal component of the β tensor oriented along the charge transfer axis (β_{zzz}); in this case, the NLO scatterers are said ''one-dimensional'' (1D) and the DR value is equal to 5. β_{HRS} and DR values were computed in the static limit ($\omega \rightarrow 0$ in eqn (13)), as well as in the dynamic regime using an incident wavelength of 1300 nm as used in the experiments.[21] All β values reported hereafter are given in atomic units (1 a.u. of $\beta = 3.6310^{-42}$ m^4 V^{-1} = 3.2063 × 10^{-53} C^3 m^3 J^{-2} = 8.641 × 10^{-33} esu) and assume a Taylor series expansion of the molecular induced dipoles with respect to the external electric fields, according to the T convention.[69]

All the computed geometrical and optical reference molecular descriptors, obtained on the considered QM optimized conformers, are collected in Table 1.

Table 1 Reference geometrical and optical descriptors for open and closed forms of BA4 used for QMD-FF validation (torsional angles δ and ξ (degrees) and distances $r_{H_O-O_{A2}}$, $r_{H_{NR}-O_{A2}}$ and $r_{O_{A1}-N_C}$ (Å), see Fig. 2 for definitions), bond length alternation (BLA, Å) and bond order alternation (BOA) along the triene bridge, calculated at the SMD:M06-2X-D3/aug-cc-pVDZ level; vertical $S_0 \rightarrow S_1$ absorption energy (ΔE_{01}, eV), first hyperpolarizability (β_{HRS}, a.u.) and depolarization ratio (DR) computed for an incident wavelength of 1300 nm and in the static limit at the SMD:M06-2X/6-311+G(d) level. For the open form, Boltzmann-averaged values calculated according the relative populations of the two conformers at room temperature are also reported

	Open			
	Conformer 1	Conformer 2	Averaged	Closed
δ_{RA}	0	0	0	47
δ_{RB}	37	46	40	108
δ_{C1}	180	180	180	—
δ_{C2}	180	180	180	—
δ_{C3}	180	180	180	—
δ_{C4}	179	179	179	—
δ_{N1}	176	1	—	142
δ_{N2}	70	80	73	170
ξ	180	180	180	—
$r_{H_O-O_{A2}}$	1.575	1.575	1.575	—
$r_{H_{NR}-O_{A2}}$	—	—	—	1.832
$r_{O_{A1}-N_C}$	11.44	11.46	11.45	4.51
BLA	−0.001	−0.006	−0.003	—
BOA	−0.017	−0.038	−0.024	—
ΔE_{01}	2.53	2.54	2.53	3.63
β_{HRS} (1300 nm)	4860	6133	5267	292
DR (1300 nm)	2.69	3.16	2.84	2.38
β_{HRS} (static)	3669	4381	3897	344
DR (static)	2.52	2.81	2.61	2.29

3 Results

3.1 QMD-FF parameterization

3.1.1 Open form. As detailed in Fig. 3a, the first step for the QMD-FF parameterization of the open form consisted in assigning specific atom types, taking into account the different (internal) chemical background experienced by each atom. Next, by looking at its chemical structure, it can be hypothesized that the open BA4 isomer is characterized by a certain degree of flexibility. Beside the trivial rotation of the methyl groups (δ_1 and δ_2) and the one around the C–OH bond (δ_{OH}, influenced by the intramolecular HB), possible dihedral distortions can also take place along the conjugated chain, *i.e.* δ_{RA}, δ_{C1}–δ_{C4}, δ_{N1}, and most likely, δ_{RB} and δ_{N2}. A summary of all possible flexible dihedrals is sketched in Fig. 3b.

The Joyce parameterization was initially carried out with varied choices concerning the flexible dihedrals and the model potential energy function (8) to the internal $r_{H_O\cdots O_{A2}}$ distance, which led to the refinement of three different sets of QMD-FF parameters, hereafter labeled as **FF1**, **FF2**, and **FF3**. Concretely, for all FFs, the stretching, bending and stiff dihedrals coordinates were described through the harmonic terms (5) and (6), whereas the flexible dihedrals δ_2, δ_{RA}, δ_{RB}, δ_{C2}, δ_{C3}, δ_{OH}, δ_{N1} and δ_{N2} were instead modeled with the Fourier-like term (7). Note that in consideration of the high barriers and the rather unfavourable local minima found in QM scans required by the training data base, dihedrals δ_{C1} and δ_{C4} were treated as flexible torsions only in the first two QMD-FFs, while in **FF3** they were considered as stiff torsions, and hence approximated through harmonic terms (see also Table 2).

Additionally, it is worth stressing that the $r_{H_O\cdots O_{A2}}$ distance between the hydroxyl proton H_O and either one of the carboxyl oxygen atoms O_{A2} is involved in two different mechanisms, and hence pivotal to determine the BA4 open form conformations: (i) the internal $H_O\cdots O_{A2}$ hydrogen bond, and (ii) the coplanarity of the C and A fragments, which in turn affects the delocalization of the electron cloud from the ring to the chain. For this reason, particular attention was paid to the LJ parameters entering eqn (8) for the H_O/O_{A2} pair, and different sets of σ^{intra} and ϵ^{intra} parameters were evaluated for each considered FF, as summarized in Table 2.

Once the LJ intramolecular parameters have been assigned, all the remaining QMD-FF parameters were determined with the Joyce code, by minimizing the standard objective function (9). All parameters are reported in Tables S2–S6 (ESI†).

Table 2 Summary of the different parameterization settings for the QMD-FFs of the DASA open form. All ϵ^{intra} and σ^{intra} parameters are reported in kJ mol^{-1} and Å, respectively. Atom labeling refers to Fig. 3

			LJ $H_O\cdots O_{A2}$		LJ $H_C\cdots H_B$		LJ $H_{C_k}\cdots H_{B_k}$	
QMD-FF	$E_{tors}(\delta_{C1})$	$E_{tors}(\delta_{C4})$	ϵ^{intra}	σ^{intra}	ϵ^{intra}	σ^{intra}	ϵ^{intra}	σ^{intra}
FF1	Cos	Cos	0.33209	1.750	0.125	2.46	—	—
FF2	Cos	Cos	15.000	1.410	0.125	2.46	0.125	2.46
FF3	Harm	Harm	15.000	1.410	0.125	2.46	0.125	2.46

3.1.2 Closed form. A specific QMD-FF was also parameterized for the closed conformer, applying the Joyce protocol, but, as discussed in the following, with slight different settings with respect to the open form, due to the very different shape and flexibility exhibited by the two isomers.

In fact, as evident in Fig. 4, the formation of the five-membered ring (*R*) from the conjugated chain (C, in open DASA, see Fig. 3) implies a chemical change in the involved atoms, which leads to different atom types and to a significant reduction of the flexible dihedrals since, apart for δ_1 and δ_2, the only allowed internal rotations are those around the σ bonds connecting the four A, C, R and M fragments, as evidenced in Fig. 4b. Yet, despite the reduced number of torsional degrees of freedom, the QM relaxed torsional scans required to build the Joyce training data set revealed a significant complexity of the conformational space accessible to the DASA closed form. Such features are mainly caused by both the steric hindrance of the rotable groups (that may ''hit'' onto each other upon rotation) and by the delicate interplay settled among different kind of ''through space'' intramolecular interactions, as the π-stacking between the A and B rings, or the internal HB between H_{NR} and O_{A2} atoms, in turn affected by possible rotations. To account for these features, the sole use of bonded valence term is clearly not sufficient, and the sum in the intramolecular non bonded energy term in eqn (8) has to be extended to a larger number of interacting pairs. Such procedure has been here performed specifically for the target molecule, manually selecting the most plausible interacting pairs, defining them through ϵ^{intra} and σ^{intra} sets tuned to reproduce a particular interaction, *e.g.* OPLS[47,48] parameters between heavy atoms of ring B and ring A for mimicking π–π stacking, or scaled parameters to simply account for steric repulsion. Such set of intramolecular LJ parameters, reported in detail in Tables S12 and S13 (ESI†), was fixed at the beginning of the Joyce parameterization, which was carried out on all the remaining harmonic and cosine force constants, according, as for the open form, to eqn (5)–(9). All parameters obtained for the closed form are reported in Tables S8–S13 (ESI†).

3.2 QMD-FF validation along the QM PES

To judge the performance of the different FFs, we have monitored some of the specific geometrical descriptors discussed in the previous sections. Firstly, **FF1** presented an issue in preserving the intramolecular hydrogen bond during the conformational dynamics occuring in MD simulations. In fact, as appears by looking at Fig. S1 (ESI†), the average $r_{H_O-O_{A2}}$ distance (>2 Å), registered in the MD runs carried out on the isolated molecules, deviates significantly from the QM reference values (1.575 Å, see also Table 1), hence suggesting that the intramolecular HB is not adequately described. To overcome this lack, the **FF2** force field was designed by refining the intramolecular LJ parameters as summarized in Table 2. The resulting change in the distribution of $r_{H_O-O_{A2}}$ from **FF1** to **FF2** can be monitored in Fig. S1 (ESI†). Notwithstanding the correct treatment of the intramolecular hydrogen bond obtained through the LJ refinement, some additional issues were found on the structures produced with **FF2**, revealed by both a structural analysis and preliminary calculations of the β responses. In fact, few snapshots revealed an anomalous twist of the backbone (see Fig. S3, ESI†), implying a distortion of the ξ dihedral, which in turn leads to a decrease of the molecular length ($r_{O_{A1}-N_C}$, see Table 1) and eventually to critical overestimation of the computed first hyperpolarizability. To avoid such inconvenience, as previously mentioned, a third QMD-FF (**FF3**) was prepared, where δ_{C1} and δ_{C4} are considered as stiff torsions and hence described with harmonic potentials (see Table 2). As a consequence, a slight reduction in the standard deviation of both ξ and the molecular elongation has been observed and illustrated in Fig. S1 and S2 (ESI†). A final validation on the intramolecular terms of **FF3** was carried out by computing selected linear and nonlinear optical properties along the trajectory in solution for the open form (Table S14, ESI†). The addition of the planarity constrains contributes to slightly reduce the standard deviation of the corresponding NLO response. The aforementioned observations have led us to the choice of **FF3** as the best fit among the built FFs for the case of open DASA. In the following, we will therefore refer to **FF3** for the discussion on the results obtained for the open form.

The parameterization of the FFs yielded standard deviations of the objective function (9) respectively of 0.8 and 1.9 kJ mol^{-1} for the open and closed isomers, and, as shown in Fig. 5, a good general agreement between the QM and QMD-FF optimized structures and vibrational modes. A more quantitative evaluation of the accuracy of the QMD-FF in reproducing the target QM data in a local harmonic approximation is given in Table 3, where the deviation between the two structures is reported in terms of internal coordinates. Excellent agreement is obtained for all coordinates in both cases, with the exception of the deviation found in the dihedrals (>10°) for the open form, which lies essentially in a misalignment of a CH_3 rotation, hence negligible to our scopes.

Besides well reproducing the optimized conformers and their oscillations around the respective equilibrium structures,

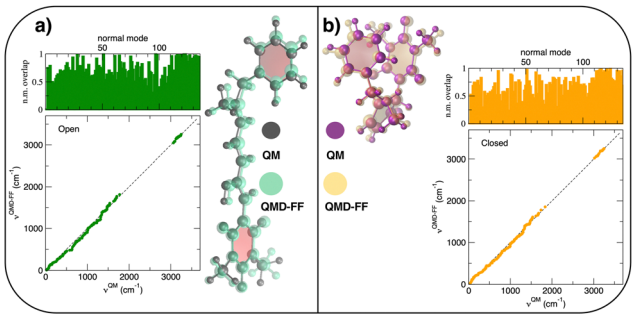

Fig. 5 (a) Open conformer: overlap between QM (gray solid spheres) and QMD-FF (transparent green spheres) optimized geometries (right) and comparison of QM and QMD-FF frequencies and normal mode overlap (left). (b) Closed conformer: overlap between QM (purple solid spheres) and QMD-FF (transparent orange spheres) optimized geometries (left) and comparison of QM and QMD-FF frequencies and normal mode overlap (right).

Table 3 RMSD between QM and QMD-FF optimized geometries in terms of bond lengths, bending angles, dihedrals and molecular normal modes (total) for the open and closed DASA isomers

Conformer	Bond lengths (Å)	Bending angles (degr)	Dihedrals (degr)	Total (Å)
Open	0.000	0.096	14.00	0.31
Closed	0.001	0.305	3.43	0.22

to reliably sample the conformational space explored by MD, it is pivotal to accurately account for the flexibility of the target molecules. For these reason all the relaxed torsional scans were recomputed at QMD-FF level, and compared to the corresponding QM profiles in Fig. 6 and 7. All the QM torsional scans computed for the open isomer appear to be well reproduced by the **FF3**, with high accuracy obtained for both the most flat profiles (δ_2, δ_{RB} and δ_{N2}) and the ones presenting higher barriers, as δ_{RA}, δ_{C2}, δ_{C3} and δ_{N1}. Furthermore, the choice of representing δ_{C1} and δ_{C4} with harmonic potentials does not

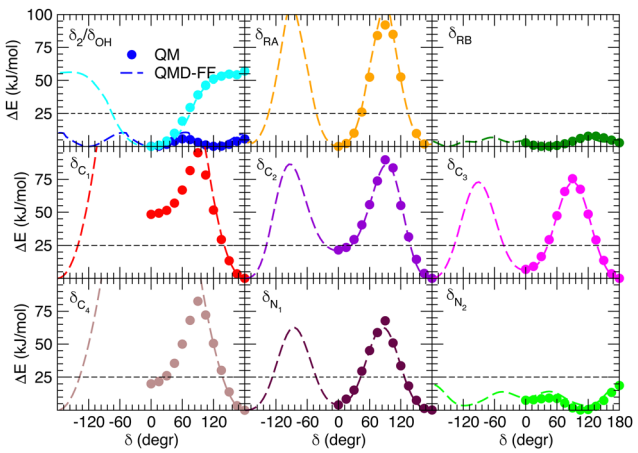

Fig. 6 Comparison of QM (full circles) and QMD-FF (**FF3**, dashed lines) relaxed torsional energy profiles for all the scanned dihedrals of the open isomer. In all panels, a dashed line is drawn to show $10k_BT$ (25 kJ mol^{-1}).

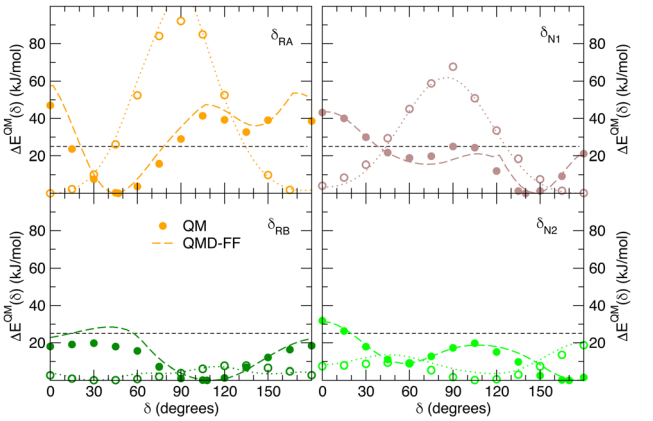

Fig. 7 Comparison of QM (full circles) and QMD-FF (dashed lines) relaxed torsional energy profiles for all the scanned dihedrals of the closed isomer. The results obtained for the same dihedrals in the open form is also drawn with empty circles (QM) and dotted lines (QMD-FF, **FF3**). In all panels, a dashed line is drawn to show $10k_BT$ (25 kJ mol^{-1}).

seem to introduce significant errors: the steepness of the repulsive branches around the minimum (180°) is in nice agreement with the one found at the QM level, whereas the QM barrier that should be crossed to populate the (high energy) local minima at 0° are located at energies well above $10k_BT$, excluding such possibility.

Fig. 7 displays the QMD-FF torsional profiles for the closed form, focusing on the four most important dihedrals by comparing them with both their QM counterparts and with the open form profiles of the same dihedrals. Notwithstanding a slightly worse agreement, due to the aforementioned complexity of the closed isomer PES, the QMD-FF appears to be capable to catch all minima and barriers of the reference QM data, and, most importantly, the completely different profiles resulting after the open-to-closed interconversion.

3.3 QMD-FF validation on geometrical properties

Choosing **FF3** as the best option among the constructed FFs, we considered 1000 structural snapshots from MD trajectories carried out in chloroform solution, and investigated first the evolution of the geometrical and electronic parameters of both the open and closed forms of BA4. Considering the open isomer, preliminary MD runs were carried out to investigate the equilbrium between the two conformers shown in Fig. 2. To this end we chose to extend the simulation time to 50 ns, yet constraining all bonds through the LINCS algorithm[70] and using an increased time step of 1 fs. Fig. 8 shows the time evolution of the δ_{N1} dihedral along such MD runs, starting either from conformer 1 or 2, as well as the relative populations of the two conformers. At room temperature, this time range is not sufficient to observe interconversion between the two conformers. However, if the temperature is raised to 500 K, conformer 2 does indeed convert to conformer 1, which is slightly favored. This result demonstrates that **FF3** is suitable for studying the conformational equilibrium in the open form of BA4, and that the interconversion barrier could be crossed

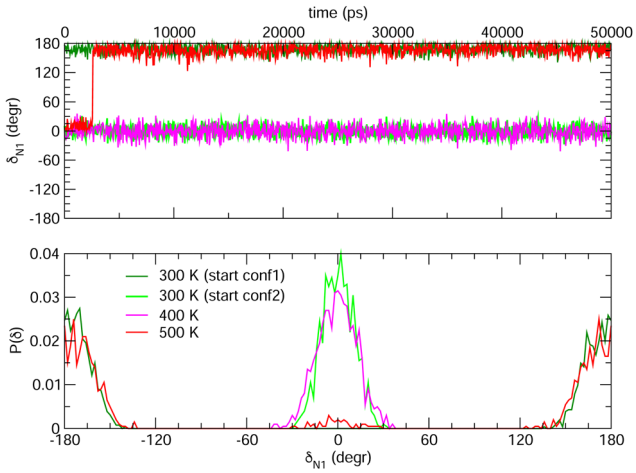

Fig. 8 Time evolution of the δ_{N1} dihedral in the open form (top) and relative populations of conformers 1 and 2 (bottom) along MD trajectories of 50 ns at various temperatures.

with longer observation times. However, since conformer 2 is not populated along the 50 s MD run performed at room temperature, the geometrical and optical properties obtained using the MD + DFT approach are compared hereafter to DFT results calculated for conformer 1.

As shown in Table 4, average values of geometrical parameters computed using the MD + DFT scheme are consistent with DFT calculations on the equilibrium geometry. However, large standard deviations are observed for dihedral angles, reflecting the high structural flexibility of the chromophore. In the open form, very broad statistical distributions are found for the δ_{RB} and δ_{N2} torsional angles (Fig. S4, ESI†), as expected from the low rotational barriers shown Fig. 6. Similarly, BLA and BOA values computed using the DFT-optimized geometry (referred to as "rigid" calculations hereafter) are very close to average values issued from the sequential MD + QM approach, while structural fluctuations induce broad distributions in the values of these two parameters, which are expected to have significant impact on the NLO responses (see Fig. 9). We should also keep in mind that our classical MD sampling leads, for high frequency motions as those behind the fluctuations of the BLA, to narrower conformational distributions as compared to a fully quantum treatment.[71] Therefore, we can expect such fluctuations to be even larger. This outcome could be achieved through methods that ensure a QM sampling, such as Path-Integral MD,[72] or by adopting hybrid quantum-classical schemes,[49] which allow treating the high frequency motions at QM level, while retaining the classical description for low frequency ones. For the purposes of the present investigation, though, the adopted fully classical sampling completely fulfills our needs in an efficient way.

We can also note that BLA and BOA, which both measure the extent of the π-conjugation in the open form, show an expected inverse correlation, as illustrated in Fig. S5 (ESI†). In our simulations, we did not find any direct correlation between the bond length/order alternation and any of the torsional parameters if taken individually (see Fig. S6, ESI†). The fact that BOA is directly correlated to BLA but not to the dihedrals may be attributed to the complete lack of conjugation effects in our FF. Such effects could be incorporated through explicit coupling terms,[37] also implemented in Joyce, but at the price of a much more complex parameterization procedure.

As found for the open form, the rotational motions associated with the terminal phenyl ring in the closed form have also low energy constraints (see Fig. 7), leading to broad distributions of the δ_{RB} and δ_{N2} angles. Compared to the open isomer, the distribution of δ_{RB} is less spread, due to the proximity of the rings RA and RB, which develop larger non-covalent van der Waals interactions that reduce the rotational flexibility of the RB fragment. Reversely, the δ_{N2} distribution is more spread in the closed form than in the open form, which comes from the greater ease of rotation around a sp^3-hybridized nitrogen compared to a sp^2-hybridized one, for which the rotation breaks the π-conjugation. We also note the larger average length of the hydrogen bond (compare $r_{H_O-O_{A2}}$ to $r_{H_{NR}-O_{A2}}$ in Table 4), consistently associated with a larger standard deviation.

Table 4 Geometric and electronic parameters computed at the SMD:M06-2X-D3/aug-cc-pVDZ level for the open and closed form, using their equilibrium geometry (conformer 1 for the open form), and using the MD + DFT scheme. All angles are in degrees, all distances in Å

	Open		Closed	
	DFT	MD + DFT	DFT	MD + DFT
δ_{RA}	0	1 ± 10	47	40 ± 6
δ_{RB}	37	80 ± 54	108	116 ± 13
δ_{C1}	180	180 ± 9	—	—
δ_{C2}	180	180 ± 11	—	—
δ_{C3}	180	180 ± 10	—	—
δ_{C4}	179	180 ± 9	—	—
δ_{N1}	176	179 ± 14	142	133 ± 62
δ_{N2}	70	82 ± 24	170	55 ± 65
ξ	180	180 ± 19	—	—
$r_{H_O-O_{A2}}$	1.575	1.675 ± 0.168	—	—
$r_{H_{NR}-O_{A2}}$	—	—	1.832	1.933 ± 0.389
BLA	−0.001	−0.001 ± 0.025	—	—
BOA	−0.017	−0.005 ± 0.066	—	—

4 Discussion

4.1 Dynamic behavior and nonlinear optical properties

We monitor in this section the fluctuations of the optical properties of the open and closed forms along the MD runs, focusing on transition energies from the ground to the lowest-energy bright excited states as well as on HRS responses at 1300 nm. The data computed at the DFT and MD + DFT levels are collected in Table 5. Note that for the open form, three structural snapshots were considered as outliers and excluded from the statistics, as they provide very low ΔE_{01} values (<2.0 eV) and massive NLO signal (>10^5 a.u.) due to frequency dispersion effects. For consistency, these outliers were removed from all statistics on the open form.

The MD + DFT probability distributions of vertical transition energies (related to the $S_0 \rightarrow S_1$ transition for the open form

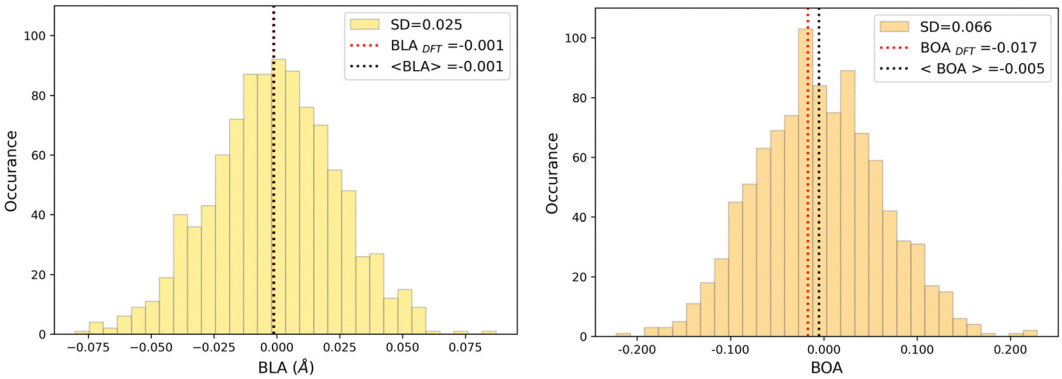

(a) BLA (b) BOA

Fig. 9 Statistical distribution of BLA (a) and BOA (b) values, calculated using the MD + DFT scheme at the SMD:M06-2X-D3/aug-cc-pVDZ level. Vertical dotted lines show the average value, and the value computed at the DFT level using the equilibrium geometry (conformer 1) of the chromophore.

Table 5 Linear and nonlinear optical properties computed at the SMD:M06-2X/6-311+G(d) level for the open and closed forms, using their equilibrium geometry (conformer 1 for the open form), and using the MD + DFT scheme. Transition energy (ΔE_{01}) and hyperpolarizability (β) values are in eV and a.u., respectively

	Open		Closed	
	DFT	MD + DFT	DFT	MD + DFT
ΔE_{01}	2.53	2.46 ± 0.10	3.63	3.62 ± 0.14
ΔE_{02}	—	—	4.17	4.07 ± 0.16
β_{HRS} (1300 nm)	4860	10969 ± 5999	292	343 ± 41
DR (1300 nm)	2.69	3.69 ± 0.77	2.38	2.21 ± 0.26
β_{HRS} (static)	3669	5525 ± 2169	335	369 ± 36
DR (static)	2.52	3.35 ± 0.74	2.03	2.15 ± 0.22

and to the $S_0 \rightarrow S_1$ and $S_0 \rightarrow S_2$ transitions for the closed form) are plotted in Fig. 10 against the absorption spectra simulated at the DFT level and the experimental spectrum for the open conformer. For the closed form, the average ΔE_{01} value calculated with the MD + DFT approach coincides with the maximal absorption energy calculated using DFT, while geometrical fluctuations induce a redshift of 0.1 eV of the $S_0 \rightarrow S_2$ transition. Similarly, the $S_0 \rightarrow S_1$ transition energy calculated for the open form using MD + DFT is 0.07 eV lower than that predicted using the S_0 equilibrium geometry of the chromophore. However, it is still significantly overestimated compared to experiments (2.46 eV *vs.* 2.18 eV as reported in ref. 21). This discrepancy can be mainly attributed to the inherent limitations of the DFT approximation, but also, to a lesser extent originates from the fact that vertical transitions provided by TD-DFT calculations are not strictly comparable to experimental maximal absorption energies. In addition, although the MD configurations sample (albeit classically) the different vibrational degrees of freedom, the MD + DFT approach fails in reproducing the band shape asymmetry observed experimentally, which broadens in the high-energy region (Fig. S7, ESI†). Similar discrepancy of the sequential MD + DFT approach was previously reported for another DASA derivative,[73] suggesting that this failure is intrinsic to the computational approach irrespective of the force field used in the MD simulations, and that more robust comparisons with experiments require the calculation of vibrationally resolved spectra using full QM approaches, as reported in ref. 74.

As illustrated in Fig. 11, geometrical fluctuations also largely affect the NLO properties, giving rise to broad distributions of β_{HRS} and DR values. The β_{HRS} distribution of the more flexible open form is much broader than that of the closed form as reflected in their standard deviation, which represents about 12% of the average value for the closed form and reaches 55% for the open form. Taking dynamic fluctuations into account for the open form also induces a dramatic increase (+125%) in β_{HRS} compared to rigid DFT calculations, whereas a much smaller increase of 17% is observed for the closed form. Accordingly, the NLO contrast upon photo-isomerization, defined as $\eta = \beta_{HRS}^{open}/\beta_{HRS}^{closed}$, also increases when accounting for structural dynamics: $\eta = 32$ from the MD + DFT approach *versus* $\eta = 17$ from rigid DFT calculations. It is also important to note that the β_{HRS} value calculated using MD + DFT is in better agreement with experimental measurements ($\beta_{HRS} = 8600 \pm 390$ a.u.). However, it is 27% overestimated, which may be attributed to an overly simple treatment of solvent effects, as interactions between the chromophore and chloroform molecules are not explicitly taken into account by the continuum solvation model.

The depolarization ratios of both DASA isomers are also spread over a broad range of values, again with a larger standard deviation in the case of the more flexible open form. The MD + DFT scheme provides a DR value larger than that issued from rigid DFT calculations and in closer agreement with experiments (DR = 5.00 ± 0.3), despite it remains significantly underestimated.

Finally, additional MD simulations were performed for the open form starting from conformer 2. The resulting distributions of the NLO responses have the same profiles as obtained from the MD sampling starting from conformer 1, leading to very similar average β_{HRS} and DR values (Fig. S8 and Table S15, ESI†). Moreover, estimating the NLO response using rigid DFT

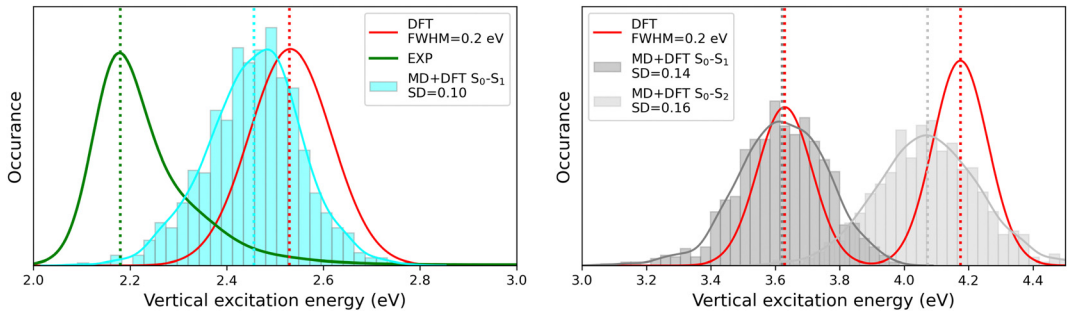

Fig. 10 Statistical distribution of the vertical $S_0 \rightarrow S_1$ transition energies of the open (left) and closed (right) forms, calculated using the MD + DFT scheme at the SMD:M06-2X/6-311+G(d) level. Vertical dotted lines indicate either average values, values computed at the DFT level using the equilibrium geometry of the chromophore (conformer 1 in the case of the open form), or experimental absorption maxima.[21] SD = standard deviation.

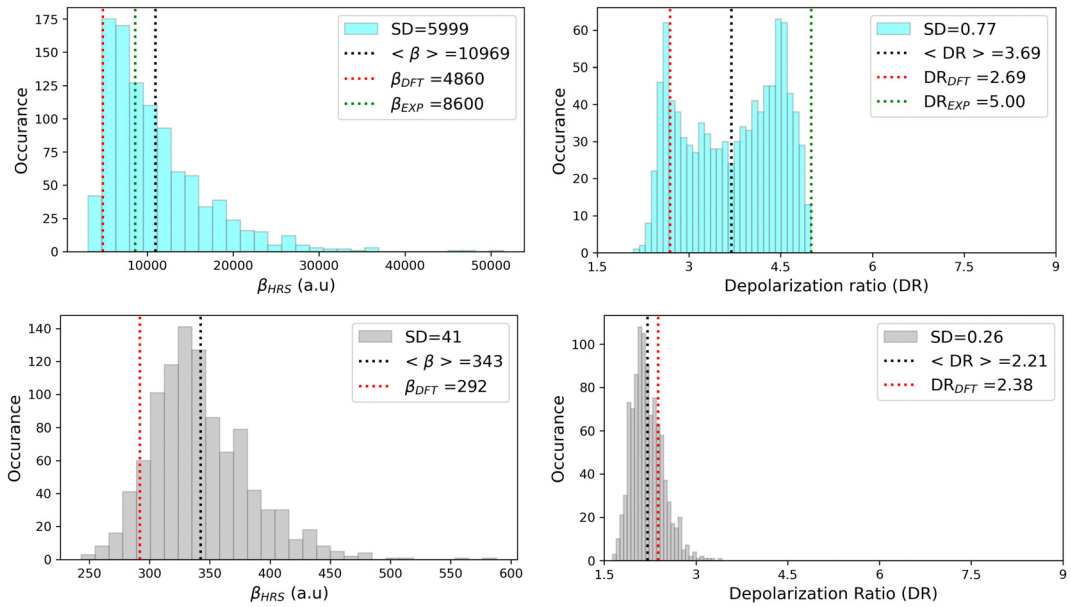

Fig. 11 Statistical distribution of the dynamic (1300 nm) HRS first hyperpolarizability and depolarization ratio of the open (top) and closed (bottom) forms, calculated using the MD + DFT scheme at the SMD:M06-2X/6-311+G(d) level. Vertical dotted lines indicate either average values, values computed at the DFT level using the equilibrium geometry of the chromophore (conformer 1 in the case of the open form), or experimental values.[21] SD = standard deviation.

calculations by weighting the responses of conformers 1 and 2 by their relative Maxwell–Boltzmann populations (Table S15, ESI†) still provides largely underestimated β_{HRS} values compared to experiments, showing that dynamic effects must be taken into account to obtain reliable estimates of the NLO responses in these systems.

4.2 Structure/NLO properties relationships in the open form

Although NLO responses of the open form are highly sensitive to geometrical fluctuations, β_{HRS} values do not show direct correlation with any of the individual torsional parameters (Fig. S9, ESI†). However, as illustrated in Fig. 12, β_{HRS} and DR values display a clear dependence on BOA and both present a minimum for BOA = 0, corresponding to the so-called cyanine limit for which the π-electron conjugation between the donor and acceptor parts is maximal. Note that, although BOA and BLA are inversely correlated (Fig. S5, ESI†), the correlation between the NLO responses and BLA is much less clear (Fig. S10, ESI†), indicating that the fluctuations of β_{HRS} and DR are better described using an electronic metric rather a structural metric of the π-conjugation.

The changes in the magnitude of the HRS hyperpolarizability with respect to the BOA fluctuations can be further rationalized using the two-state approximation (TSA).[75] This approximation is based on the perturbative sum-over-state expansion of the second-order NLO response and assumes that the only non-negligible contribution arises from the first dipole-allowed electronic excited state (S_1), leading to a very simple expression of the dynamic HRS hyperpolarizability in terms of spectroscopic quantities. Limiting the β tensor to its single diagonal β_{zzz} component, with z the charge-transfer axis of the molecule, it yields:

$$\beta_{HRS}^{TSA} \simeq \sqrt{\frac{6}{35}}\beta_{zzz}^{TSA} = \sqrt{\frac{216}{35}}\frac{\mu_{01}^2|\Delta\mu_{01}|}{\Delta E_{01}^2}F(\omega) \qquad (16)$$

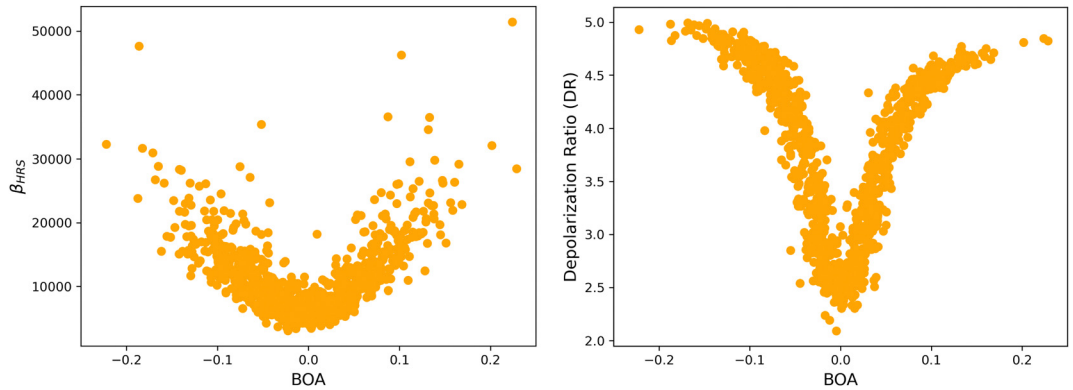

Fig. 12 Distribution of β_{HRS} (left) and DR (right) values as a function of the bond order alternation (BOA) for the open form.

where ΔE_{01} is the $S_0 \rightarrow S_1$ excitation energy, μ_{01} is the associated z-component of the transition dipole, and $\Delta\mu_{01} = |\mu^z_{S_1} - \mu^z_{S_0}|$ is the change in the permanent dipole moment between the two electronic states. $F(\omega)$ is a factor accounting for frequency dispersion, which depends on the energy of the incident photons ($\hbar\omega$ = 0.95 eV for a 1300 nm wavelength):

$$F(\omega) = \frac{\Delta E_{01}^4}{\left(\Delta E_{01}^2 - (\hbar\omega)^2\right)\left(\Delta E_{01}^2 - (2\hbar\omega)^2\right)} \quad (17)$$

The suitability of the TSA for describing the effect of structural fluctuations on the molecular first hyperpolarizability is demonstrated in Fig. S11 (ESI†), which shows a good linear correlation between the β_{HRS} values calculated at the TDDFT level and those estimated using eqn 16 in both the static and the dynamic regimes. Moreover, the frequency dispersion factor estimated using eqn 17 provides a good estimate of the resonance effects in the range of ΔE_{01} values spanned by the dynamics (Fig. S11, ESI†). Although neither ΔE_{01} nor μ_{01} correlate with BOA (Fig. S12, ESI†), Fig. 13a clearly shows that $\Delta\mu_{01}$ linearly decreases with BOA, and is equal to zero when BOA = 0. We can therefore conclude that the variations of β_{HRS} shown in Fig. 12 are mainly driven by the variations of $\Delta\mu_{01}$, as further illustrated in Fig. 13b.

In turn, the variation of $\Delta\mu_{01}$ with respect to BOA can be rationalized by means of the valence bond-charge transfer (VB-CT) model,[76–79] which assumes that the (orthogonal) wavefunctions of the electronic ground and excited states, $|\psi_{S_0}\rangle$ and $|\psi_{S_1}\rangle$, can be expressed as linear combinations of two VB resonance structures, namely a weakly polar $|DA\rangle$ form and a highly polar zwitterionic form $|D^+A^-\rangle$ corresponding to the transfer of one electron from the amine donor (D) to the barbituric acceptor (A):

$$\begin{aligned} |\psi_{S_0}\rangle &= \sqrt{1-\kappa}|DA\rangle + \sqrt{\kappa}|D^+A^-\rangle \\ |\psi_{S_1}\rangle &= \sqrt{\kappa}|DA\rangle - \sqrt{1-\kappa}|D^+A^-\rangle \end{aligned} \quad (18)$$

where κ ranges between 0 and 1 and measures the π-electron charge transfer between the D and A units in the ground state. By definition, the cyanine limit (BOA = 0) is associated to a value of κ equal to 1/2, which corresponds to equal weights for the $|DA\rangle$ and $|D^+A^-\rangle$ forms in both electronic states. According to the VB-CT model and assuming no dipolar coupling between the $|DA\rangle$ and $|D^+A^-\rangle$ forms ($\langle DA|\hat{\mu}|D^+A^-\rangle = 0$), the dipole moment variation upon the $S_0 \rightarrow S_1$ transition can be written as:

$$\Delta\mu_{01} = (2\kappa - 1)\mu_{DA} + (1 - 2\kappa)\mu_{D^+A^-} \quad (19)$$

where μ_{DA} and $\mu_{D^+A^-}$ are the dipole moments of the $|DA\rangle$ and $|D^+A^-\rangle$ forms, respectively. Therefore, $\Delta\mu_{01} = 0$ if $\kappa = 1/2$, *i.e.* if BOA = 0, as it is observed in Fig. 13a. The contribution of the excited state participating the most to the NLO response is thus

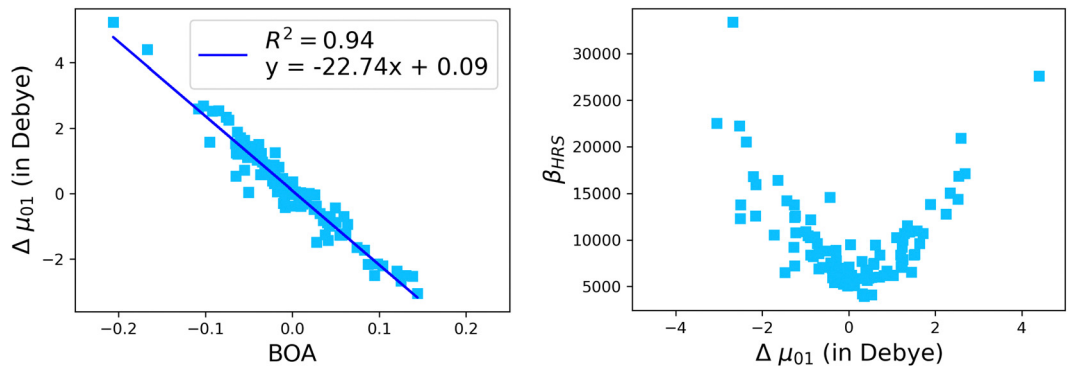

Fig. 13 Evolution of $\Delta\mu_{01}$ of the open form as a function of the BOA (left), and evolution of β_{HRS} of the open form as a function of $\Delta\mu_{01}$. The calculations have been performed for 100 structural snapshots taken every 10 picoseconds of the MD trajectory.

cancelled out in the cyanine limit, which explains the minimum reached by the β_{HRS} values in Fig. 12a, and the reason why taking geometric fluctuations into account increases the magnitude of the second-order NLO response compared with rigid DFT calculations, which only consider a single cyanine-type conformer.

The evolution of the depolarization ratio DR with respect to the BOA shown in Fig. 12b can also be simply rationalized, considering a few simplifications. First, let's assume that, in addition to SHG (degenerated sum-frequency generation), Kleinman's permutation rules apply, so that $\beta_{ijk} = \beta_{ikj} = \beta_{jik} = \beta_{jki} = \beta_{kij} = \beta_{kji}$ for any component of the molecular β tensor. Note that Kleinman's conditions require to be far from any resonance between the absorption bands of the chromophore and the second harmonic light at 650 nm ($\sim$1.9 eV), which is a reasonable approximation according to the absorption spectrum shown in Fig. 10a. Second, let's assume that the chromophore possesses a pseudo-planar C_{2v} symmetry, as it was considered in number of previous studies for push–pull systems.[80–83] With z the axis parallel to the C_2 (charge transfer) axis and x the transverse direction within the molecular plane, one has: ($\beta_{xxx} = \beta_{xyy} = \beta_{xzz} = \beta_{xyz} = \beta_{yxx} = \beta_{yyy} = \beta_{yzz} = 0$, $\beta_{zzz} \neq 0$, and $\beta_{zxx} \neq 0$). Furthermore, we assume that $\beta_{zyy} = 0$, as this tensor component is expected to be small with respect to β_{zzz} and β_{zxx}. In that case, the depolarization ratio can be simply expressed as a function of the ratio $R = \beta_{zxx}/\beta_{zzz}$ between the only two non-zero β components:

$$\mathrm{DR}(C_{2v}) = \frac{15 + 18R + 27R^2}{3 - 2R + 11R^2} \qquad (20)$$

According to eqn (20), DR converges towards the value of $27/11 \simeq 2.45$ when $R \to \infty$, *i.e.* when β_{zzz} (and thus β_{HRS}) tends to zero. This value of $\simeq$2.45 corresponds to the minimum reached by the DR values when BOA = 0 in Fig. 12, and is close to the DR value of 2.69 calculated for the equilibrium geometry of the chromophore (Table 5). Reversely, $R = 0$ corresponds to DR = 5, which is typical of "1D" push–pull chromophores in which the β_{zzz} component dominates the β tensor. One can see in Fig. 12b that this situation corresponds to the largest absolute values of BOA, and therefore that dynamic fluctuations enhance the 1D NLO character of the chromophore.

The validity of the above considerations for the open form of BA4 is demonstrated in Fig. 14a, which illustrates the evolution with BOA of absolute R values calculated without assuming Kleinman or full C_{2v} symmetry (see ESI,† for details on the calculation of R). One can indeed observe that $|R|$ diverges when BOA equals 0, whereas it vanishes for large absolute BOA values. Fig. 14b further shows that the evolution of DR with respect to R qualitatively follows the ideal Kleinman-C_{2v} behavior, although computed DR values are limited in the 2.1–5.0 range, whereas they show a greater amplitude (from 1.5 to 6.75) for pure C_{2v} systems.

5 Conclusion

In this work, we carried out classical MD simulations on both the open and closed isomers of a DASA derivative in chloroform solution, by using specific force fields derived by means of the Joyce protocol. Subsequent DFT calculations performed on structural snapshots extracted from the MD trajectories enabled us to demonstrate the significant impact of geometric fluctuations on the second-order NLO responses associated with hyper-Rayleigh scattering experiments. In particular, taking structural dynamics into account considerably increases the first hyperpolarizability of the NLO-active open form compared with DFT calculations performed on Maxwell–Boltzmann-weighted sets of conformers, and provides an average β_{HRS} value in better agreement with experimental data. However, the depolarization ratio predicted by the MD + DFT scheme remains significantly underestimated with respect to experiments, a discrepancy that may be attributed to the use of a continuum solvation model to describe solute–solvent interactions. Further work implying calculations of the NLO properties of the DASA chromophore surrounded by explicit chloroform molecules is in progress.

MD + DFT calculations also revealed that the large enhancement of β_{HRS} induced by the dynamic fluctuations in the open isomer are correlated with the changes in the bond order

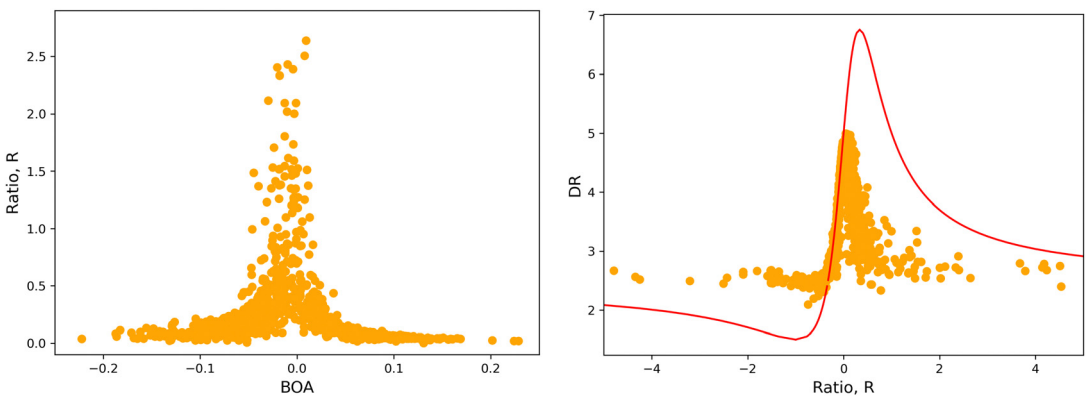

Fig. 14 (left) Evolution of $|R|$ as a function of BOA (truncated to $|R| < 3$); (right) evolution of DR with respect to R in the case of an ideal Kleinman C_{2v} symmetry (eqn (20), red line) and using computed values (orange dots).

alternation along the π-conjugated bridge linking the amine donor and the barbituric acid acceptor. Structural distortions take the molecule out of its cyanine-type equilibrium geometry, moving the bond order alternation away from its zero value and increasing the second-order NLO response. An interesting correlation was also found between the bond order alternation and the depolarization ratio, which could be qualitatively rationalized by using simple symmetry assumptions.

At last, this work demonstrates the reliability of the sequential application of classical MD and DFT calculations for the accurate prediction of the NLO responses of conjugated organic molecular systems in dilute solution. In addition, this computational strategy enables us to better understand the important role of dynamic fluctuations and the interaction between electron conjugation within the molecule and its NLO properties.

Conflicts of interest

There are no conflicts to declare.

Acknowledgements

We thank Dr Eduard Matito for kindly providing us the ESI-3D code for computing the bond orders. A. D. and F. C. thank Prof. Benoît Champagne for helpful discussions. C. N. acknowledges the DIPC for his postdoctoral PhD grant. This work was supported by the French National Research Agency (grant number ANR-20-CE29-0009-01) and by the Transnational Common Laboratory QuantumChemPhys (Theoretical Chemistry and Physics at the Quantum Scale, grant number ANR-10-IDEX-03-02) established between the Université de Bordeaux (UB), Euskal Herriko Unibertsitatea (UPV/EHU) and the Donostia International Physics Center (DIPC). Calculations were performed using the computing facilities provided by the Mésocentre de Calcul Intensif Aquitain (MCIA) of UB and of the Université de Pau et des Pays de lAdour. J. C. thanks the Ministerio de Universidades, Plan de Recuperación, Transformación y Resiliencia and UAM for funding the research stay in Pisa with a requalification program (CA2/RSUE/2021-00890). G. P. thanks the financial support from ICSC – Centro Nazionale di Ricerca in High Performance Computing, Big Data and Quantum Computing, funded by European Union – NextGenerationEU – PNRR, Missione 4 Componente 2 Investimento 1.4.

References

1 S. Helmy, F. A. Leibfarth, S. Oh, J. E. Poelma, C. J. Hawker and J. R. De Alaniz, Photoswitching using visible light: a new class of organic photochromic molecules, *J. Am. Chem. Soc.*, 2014, **136**, 8169–8172.

2 S. Helmy, S. Oh, F. A. Leibfarth, C. J. Hawker and J. Read de Alaniz, Design and Synthesis of Donor–Acceptor Stenhouse Adducts: A Visible Light Photoswitch Derived from Furfural, *J. Org. Chem.*, 2014, **79**, 11316–11329.

3 J. R. Hemmer, S. O. Poelma, N. Treat, Z. A. Page, N. D. Dolinski, Y. J. Diaz, W. Tomlinson, K. D. Clark, J. P. Hooper, C. Hawker and J. Read De Alaniz, Tunable Visible and Near Infrared Photoswitches, *J. Am. Chem. Soc.*, 2016, **138**, 13960–13966.

4 M. M. Lerch, S. J. Wezenberg, W. Szymanski and B. L. Feringa, Unraveling the Photoswitching Mechanism in Donor-Acceptor Stenhouse Adducts, *J. Am. Chem. Soc.*, 2016, **138**, 6344–6347.

5 N. Mallo, P. T. Brown, H. Iranmanesh, T. S. C. MacDonald, M. J. Teusner, J. B. Harper, G. E. Ball and J. E. Beves, Photochromic switching behaviour of donoracceptor Stenhouse adducts in organic solvents, *Chem. Commun.*, 2016, **52**, 13576–13579.

6 M. D. Donato, M. M. Lerch, A. Lapini, A. D. Laurent, A. Iagatti, L. Bussotti, S. P. Ihrig, M. Medved, D. Jacquemin, W. Szymański, W. J. Buma, P. Foggi and B. L. Feringa, Shedding Light on the Photoisomerization Pathway of Donor–Acceptor Stenhouse Adducts, *J. Am. Chem. Soc.*, 2017, **139**, 15596–15599.

7 M. M. Lerch, W. Szymański and B. L. Feringa, The (photo)-chemistry of Stenhouse photoswitches: guiding principles and system design, *Chem. Soc. Rev.*, 2018, **47**, 1910–1937.

8 M. M. Lerch, M. Di Donato, A. D. Laurent, M. Medved', A. Iagatti, L. Bussotti, A. Lapini, W. J. Buma, P. Foggi, W. Szymański and B. L. Feringa, Solvent Effects on the Actinic Step of Donor–Acceptor Stenhouse Adduct Photoswitching, *Angew. Chem., Int. Ed.*, 2018, **57**, 8063–8068.

9 R. F. A. Gomes, J. A. S. Coelho and C. A. M. Afonso, Synthesis and Applications of Stenhouse Salts and Derivatives, *Chem. – Eur. J.*, 2018, **24**, 9170–9186.

10 J. R. Hemmer, Z. A. Page, K. D. Clark, F. Stricker, N. D. Dolinski, C. J. Hawker and J. Read De Alaniz, Controlling Dark Equilibria and Enhancing Donor-Acceptor Stenhouse Adduct Photoswitching Properties through Carbon Acid Design, *J. Am. Chem. Soc.*, 2018, **140**, 10425–10429.

11 C. García-Iriepa, M. Marazzi and D. Sampedro, From Light Absorption to Cyclization: Structure and Solvent Effects in Donor-Acceptor Stenhouse Adducts, *ChemPhotoChem*, 2019, **3**, 866–873.

12 H. Zulfikri, M. A. J. Koenis, M. M. Lerch, M. D. Donato, W. Szymański, C. Filippi, B. L. Feringa and W. J. Buma, Taming the complexity of donor-acceptor stenhouse adducts: Infrared motion pictures of the complete switching pathway, *J. Am. Chem. Soc.*, 2019, **141**, 7376–7384.

13 M. Ugandi and M. Roemelt, An Ab Initio Computational Study of Electronic and Structural Factors in the Isomerization of Donor-Acceptor Stenhouse Adducts, *J. Phys. Chem. A*, 2020, **124**, 7756–7767.

14 D. M. Sanchez, U. Raucci, K. N. Ferreras and T. J. Martínez, Putting Photomechanical Switches to Work: An Ab Initio Multiple Spawning Study of Donor-Acceptor Stenhouse Adducts, *J. Phys. Chem. Lett.*, 2020, **11**, 7901–7907.

15 C. Xiong, G. Xue, L. Mao, L. Gu, C. He, Y. Zheng and D. Wang, Carbon Spacer Strategy: Control the Photoswitching Behavior

of Donor-Acceptor Stenhouse Adducts, *Langmuir*, 2021, **37**, 802–809.

16 S. W. Connolly, R. Tiwari, S. J. Holder and H. J. Shepherd, A simple strategy to overcome concentration dependence of photoswitching properties in donor-acceptor Stenhouse adducts, *Phys. Chem. Chem. Phys.*, 2021, **23**, 2775–2779.

17 S. O. Poelma, S. S. Oh, S. Helmy, A. S. Knight, G. L. Burnett, H. T. Soh, C. J. Hawker and J. Read de Alaniz, Controlled drug release to cancer cells from modular one-photon visible light-responsive micellar system, *Chem. Commun.*, 2016, **52**, 10525–10528.

18 M. Clerc, S. Sandlass, O. Rifaie-Graham, J. A. Peterson, N. Bruns, J. Read de Alaniz and L. F. Boesel, Visible light-responsive materials: the (photo)chemistry and applications of donor–acceptor Stenhouse adducts in polymer science, *Chem. Soc. Rev.*, 2023, **52**, 8245–8294.

19 C. Tonnelé, B. Champagne, L. Muccioli and F. Castet, Second-order nonlinear optical properties of Stenhouse photoswitches: insights from density functional theory, *Phys. Chem. Chem. Phys.*, 2018, **20**, 27658–27667.

20 Y. Yao, H.-L. Xu and Z.-M. Su, Switching of second-order nonlinear response effected by different acceptors: The impacts of environment and frequency dispersion, *Dyes Pigm.*, 2021, **193**, 109502.

21 S. Dubuis, A. Dellai, C. Courdurié, J. Owona, A. Kalafatis, L. Vellutini, E. Genin, V. Rodriguez and F. Castet, Nonlinear Optical Responses of Photoswitchable Donor–Acceptor Stenhouse Adducts, *J. Am. Chem. Soc.*, 2023, **145**, 10861–10871.

22 F. Castet, C. Tonnelé, L. Muccioli and B. Champagne, Predicting the Second-Order Nonlinear Optical Responses of Organic Materials: the Role of Dynamics, *Acc. Chem. Res.*, 2022, **55**, 3716–3726.

23 K. Coutinho and S. Canuto, Solvent Effects from a Sequential Monte Carlo – Quantum Mechanical Approach, in *Advances in Quantum Chemistry*, ed. P.-O. Löwdin, J. R. Sabin, M. C. Zerner, J. Karwowski and M. Karelson, Academic Press, 1997, vol. 28, pp. 89–105.

24 R. C. Barreto, K. Coutinho, H. C. Georg and S. Canuto, Combined Monte Carlo and quantum mechanics study of the solvatochromism of phenol in water. The origin of the blue shift of the lowest π–π* transition, *Phys. Chem. Chem. Phys.*, 2009, **11**, 1388–1396.

25 N. De Mitri, S. Monti, G. Prampolini and V. Barone, Absorption and Emission Spectra of a Flexible Dye in Solution: A Computational Time-Dependent Approach, *J. Chem. Theory Comput.*, 2013, **9**, 4507–4516.

26 I. Cacelli, A. Ferretti and G. Prampolini, Perturbative multi-reference configuration interaction (CI-MRPT2) calculations in a focused dynamical approach: A computational study of solvatochromism in pyrimidine, *J. Phys. Chem. A*, 2015, **119**, 5250–5259.

27 J. Quertinmont, B. Champagne, F. Castet and M. Hidalgo Cardenuto, Explicit versus Implicit Solvation Effects on the First Hyperpolarizability of an Organic Biphotochrome, *J. Phys. Chem. A*, 2015, **119**, 5496–5503.

28 K. Pielak, C. Tonnelé, L. Sanguinet, E. Cariati, S. Righetto, L. Muccioli, F. Castet and B. Champagne, Dynamical Behavior and Second Harmonic Generation Responses in Acido-Triggered Molecular Switches, *J. Phys. Chem. C*, 2018, **122**, 26160–26168.

29 T. Giovannini, M. Ambrosetti and C. Cappelli, A polarizable embedding approach to second harmonic generation (SHG) of molecular systems in aqueous solutions, *Theor. Chem. Acc.*, 2018, **137**, 74.

30 T. N. Ramos, S. Canuto and B. Champagne, Unraveling the Electric Field-Induced Second Harmonic Generation Responses of Stilbazolium Ion Pairs Complexes in Solution Using a Multiscale Simulation Method, *J. Chem. Inf. Model.*, 2020, **60**, 4817–4826.

31 J. Seibert, B. Champagne, S. Grimme and M. de Wergifosse, Dynamic Structural Effects on the Second-Harmonic Generation of Tryptophane-Rich Peptides and Gramicidin A, *J. Phys. Chem. B*, 2020, **124**, 2568–2578.

32 T. Hrivnák, H. Reis, P. Neogrády, R. Zaleśny and M. Medved', Accurate Nonlinear Optical Properties of Solvated para-Nitroaniline Predicted by an Electrostatic Discrete Local Field Approach, *J. Phys. Chem. B*, 2020, **124**, 10195–10209.

33 T. N. Ramos, F. Castet and B. Champagne, Second Harmonic Generation Responses of Ion Pairs Forming Dimeric Aggregates, *J. Phys. Chem. B*, 2021, **125**, 3386–3397.

34 C. Naim, R. Vangheluwe, I. Ledoux-Rak, B. Champagne, C. Tonnelé, M. BlanchardDesce, E. Matito and F. Castet, Electric-field induced second harmonic generation responses of push–pull polyenic dyes: experimental and theoretical characterizations, *Phys. Chem. Chem. Phys.*, 2023, **25**, 13978–13988.

35 C. Bouquiaux, P. Beaujean, T. N. Ramos, F. Castet, V. Rodriguez and B. Champagne, First hyperpolarizability of the di-8-ANEPPS and DR1 nonlinear optical chromophores in solution. An experimental and multi-scale theoretical chemistry study, *J. Chem. Phys.*, 2023, **159**, 174307.

36 I. Cacelli and G. Prampolini, Parametrization and Validation of Intramolecular Force Fields Derived from DFT Calculations, *J. Chem. Theory Comput.*, 2007, **3**, 1803–1817.

37 J. Cerezo, G. Prampolini and I. Cacelli, Developing accurate intramolecular force fields for conjugated systems through explicit coupling terms, *Theor. Chem. Acc.*, 2018, **137**, 80.

38 G. Prampolini, L. G. D. Silveira, J. G. Vilhena and P. R. Livotto, Predicting Spontaneous Orientational Self-Assembly: In Silico Design of Materials with Quantum Mechanically Derived Force Fields, *J. Phys. Chem. Lett.*, 2022, **13**, 243–250.

39 N. Mallo, E. D. Foley, H. Iranmanesh, A. D. Kennedy, E. T. Luis, J. Ho, J. B. Harper and J. E. Beves, Structure-function relationships of donor-acceptor Stenhouse adduct photochromic switches, *Chem. Sci.*, 2018, **9**, 8242–8252.

40 M. J. Frisch, *et al.*, *Gaussian 16 Revision C.01*, Gaussian Inc., Wallingford CT, 2016.

41 Y. Zhao and D. G. Truhlar, The M06 suite of density functionals for main group thermochemistry, thermochemical

kinetics, noncovalent interactions, excited states, and transition elements: Two new functionals and systematic testing of four M06-class functionals and 12 other function, *Theor. Chem. Acc.*, 2008, **120**, 215–241.

42 S. Grimme, J. Antony, S. Ehrlich and H. Krieg, A consistent and accurate ab initio parametrization of density functional dispersion correction (DFT-D) for the 94 elements H-Pu, *J. Chem. Phys.*, 2010, **132**, 154104.

43 A. V. Marenich, C. J. Cramer and D. G. Truhlar, Universal Solvation Model Based on Solute Electron Density and on a Continuum Model of the Solvent Defined by the Bulk Dielectric Constant and Atomic Surface Tensions, *J. Phys. Chem. B*, 2009, **113**, 6378–6396.

44 I. Cacelli, A. Cimoli, P. R. Livotto and G. Prampolini, An Automated Approach for the Parameterization of Accurate Intermolecular Force-Fields: Pyridine as a Case Study, *J. Chem. Theory Comput.*, 2012, **33**, 1055.

45 G. Prampolini, P. R. Livotto and I. Cacelli, Accuracy of Quantum Mechanically Derived Force-Fields Parameterized from Dispersion-Corrected DFT Data: The Benzene Dimer as a Prototype for Aromatic Interactions, *J. Chem. Theory Comput.*, 2015, **11**, 5182–5196.

46 G. Prampolini, F. Ingrosso, J. Cerezo, A. Iagatti, P. Foggi and M. Pastore, Shortand Long-Range Solvation Effects on the Transient UV–Vis Absorption Spectra of a Ru(II)–Polypyridine Complex Disentangled by Nonequilibrium Molecular Dynamics, *J. Phys. Chem. Lett.*, 2019, **10**, 2885–2891.

47 W. L. Jorgensen, D. S. Maxwell and J. Tirado-rives, Development and Testing of the OPLS All-Atom Force Field on Conformational Energetics and Properties of Organic Liquids, *J. Am. Chem. Soc.*, 1996, **118**, 11225–11236.

48 W. L. Jorgensen and J. Tirado-Rives, Potential Energy Functions for Atomic-Level Simulations of Water and Organic and Biomolecular Systems, *Proc. Natl. Acad. Sci. U. S. A.*, 2005, **102**, 6665–6670.

49 J. Cerezo, D. Aranda, F. J. Avila Ferrer, G. Prampolini and F. Santoro, AdiabaticMolecular Dynamics Generalized Vertical Hessian Approach: A Mixed Quantum Classical Method to Compute Electronic Spectra of Flexible Molecules in the Condensed Phase, *J. Chem. Theory Comput.*, 2020, **16**, 1215–1231.

50 I. Cacelli, J. Cerezo, N. De Mitri and G. Prampolini, Joyce2.10, a Fortran 77 code for intra-molecular force field parameterization, available free of charge at **https://www.iccom.cnr.it/en/joyce-2/**, last consulted May 2022. 2019.

51 R. Pawlak, J. G. Vilhena, P. D'Astolfo, X. Liu, G. Prampolini, T. Meier, T. Glatzel, J. A. Lemkul, R. Häner, S. Decurtins, A. Baratoff, R. Pérez, S.-X. Liu and E. Meyer, Sequential Bending and Twisting around C–C Single Bonds by Mechanical Lifting of a Pre-Adsorbed Polymer, *Nano Lett.*, 2020, **20**, 652–657.

52 A. Segalina, J. Cerezo, G. Prampolini, F. Santoro and M. Pastore, Accounting for Vibronic Features through a Mixed Quantum-Classical Scheme: Structure, Dynamics, and Absorption Spectra of a Perylene Diimide Dye in Solution, *J. Chem. Theory Comput.*, 2020, **16**, 7061–7077.

53 M. J. Abraham, T. Murtola, R. Schulz, S. Páll, J. C. Smith, B. Hess and E. Lindahl, GROMACS: High performance molecular simulations through multi-level parallelism from laptops to supercomputers, *SoftwareX*, 2015, **1–2**, 19–25.

54 H. J. C. Berendsen, J. P. M. Postma, W. F. van Gunsteren, A. DiNola and J. R. Haak, Molecular dynamics with coupling to an external bath, *J. Chem. Phys.*, 1984, **81**, 3684–3690.

55 G. Bussi, D. Donadio and M. Parrinello, Canonical sampling through velocity rescaling, *J. Chem. Phys.*, 2007, **126**, 014101.

56 M. Parrinello and A. Rahman, Polymorphic transitions in single crystals: A new molecular dynamics method, *J. Appl. Phys.*, 1981, **52**, 7182–7190.

57 R. F. W. Bader, *Atoms in Molecules: A Quantum Theory*, Oxford University Press, Oxford, 1990.

58 T. A. Keith, *AIMAll (Version 14.11.23)*, TK Gristmill Software, Overland Park KS, USA, 2014.(aim.tkgristmill.com).

59 E. Matito, ESI-3D: Electron Sharing Indices Program for Molecular Space Partitioning. 2023; nstitute of Computational chemistry and Catalysis (IQCC), University of Girona, Catalonia, Spain (2006–2015) and Donostia International Physics Center (DIPC), Euskadi, Spain (2015-2023).

60 E. Matito, M. Solà, P. Salvador and M. Duran, Electron sharing indexes at the correlated level. Application to aromaticity calculations, *Faraday Discuss.*, 2007, **135**, 325–345.

61 E. Matito, M. Duran and M. Solà, The aromatic fluctuation index (FLU): a new aromaticity index based on electron delocalization, *J. Chem. Phys.*, 2005, **122**, 014109.

62 R. F. W. Bader and M. E. Stephens, Spatial localization of the electronic pair and number distributions in molecules, *J. Am. Chem. Soc.*, 1975, **97**, 7391–7399.

63 X. Fradera, M. A. Austen and R. F. W. Bader, The Lewis Model and Beyond, *J. Phys. Chem. A*, 1999, **103**, 304–314.

64 D. Jacquemin, E. A. Perpète, I. Ciofini and C. Adamo, Assessment of recently developed density functional approaches for the evaluation of the bond length alternation in polyacetylene, *Chem. Phys. Lett.*, 2005, **405**, 376–381.

65 D. Jacquemin, A. Femenias, H. Chermette, I. Ciofini, C. Adamo, J.-M. André and E. A. Perpète, Assessment of Several Hybrid DFT Functionals for the Evaluation of Bond Length Alternation of Increasingly Long Oligomers, *J. Phys. Chem. A*, 2006, **110**, 5952–5959.

66 D. Jacquemin, E. A. Perpète, H. Chermette, I. Ciofini and C. Adamo, Comparison of theoretical approaches for computing the bond length alternation of polymethineimine, *Chem. Phys.*, 2007, **332**, 79–85.

67 M. Torrent-Sucarrat, S. Navarro, F. P. Cossío, J. M. Anglada and J. M. Luis, Relevance of the DFT method to study expanded porphyrins with different topologies, *J. Comput. Chem.*, 2017, **38**, 2819–2828.

68 I. Casademont-Reig, T. Wöller, J. Contreras-García, M. Alonso, M. TorrentSucarrat and E. Matito, New electron delocalization tools to describe the aromaticity in porphyrinoids, *Phys. Chem. Chem. Phys.*, 2018, **20**, 2787–2796.

69 H. Reis, Problems in the comparison of theoretical and experimental hyperpolarizabilities revisited, *J. Chem. Phys.*, 2006, **125**, 014506.

70 B. Hess, B. Bekker, H. Berendsen and J. G. E. M. Fraaije, LINCS: a linear constraint solver for molecular simulations, *J. Comput. Chem.*, 1997, **18**, 1463–1472.
71 J. Cerezo, F. Santoro and G. Prampolini, Comparing classical approaches with empirical or quantum-mechanically derived force fields for the simulation electronic lineshapes: application to coumarin dyes, *Theor. Chem. Acc.*, 2016, **135**, 143 (1–21).
72 T. E. Markland and M. Ceriotti, Nuclear quantum effects enter the mainstream, *Nat. Rev. Chem.*, 2018, **2**, 0109.
73 C. García-Iriepa and M. Marazzi, Level of theory and solvent effects on DASA absorption properties prediction: Comparing TD-DFT, CASPT2 and NEVPT2, *Materials*, 2017, **10**, 1025.
74 A. D. Laurent, M. Medved and D. Jacquemin, Using Time-Dependent Density Functional Theory to Probe the Nature of Donor–Acceptor Stenhouse Adduct Photochromes, *ChemPhysChem*, 2016, 1846–1851.
75 J. L. Oudar and D. S. Chemla, Hyperpolarizabilities of the nitroanilines and their relations to the excited state dipole moment, *J. Chem. Phys.*, 1976, **66**, 2664–2668.
76 D. Lu, G. Chen, J. W. Perry and W. A. I. Goddard, Valence-Bond Charge-Transfer Model for Nonlinear Optical Properties of Charge-Transfer Organic Molecules, *J. Am. Chem. Soc.*, 1994, **116**, 10679–10685.
77 F. Meyers, S. R. Marder, B. M. Pierce and J. L. Bredas, Electric Field Modulated Nonlinear Optical Properties of Donor-Acceptor Polyenes: Sum-Over-States Investigation of the Relationship between Molecular Polarizabilities (.alpha.,.beta., and.gamma.) and Bond Length Alternation, *J. Am. Chem. Soc.*, 1994, **116**, 10703–10714.
78 M. Barzoukas, C. Runser, A. Fort and M. Blanchard-Desce, A two-state description of (hyper) polarizabilities of push-pull molecules based on a two-form model, *Chem. Phys. Lett.*, 1996, **257**, 531–537.
79 P. Beaujean and B. Champagne, Unraveling the Symmetry Effects on the Second-Order Nonlinear Optical Responses of Molecular Switches: The Case of Ruthenium Complexes, *Inorg. Chem.*, 2022, **61**, 1928–1940.
80 L. Sanguinet, J. L. Pozzo, V. Rodriguez, F. Adamietz, F. Castet, L. Ducasse and B. Champagne, Acido- and Photo-triggered NLO Properties Enhancement, *J. Phys. Chem. B*, 2005, **109**, 11139–11150.
81 A. Plaquet, M. Guillaume, B. Champagne, L. Rougier, F. Mancois, V. Rodriguez, J.-L. Pozzo, L. Ducasse and F. Castet, Investigation on the Second-Order Nonlinear Optical Responses in the Keto-Enol Equilibrium of Anil Derivatives, *J. Phys. Chem. C*, 2008, **112**, 5638–5645.
82 F. Mancois, J.-L. Pozzo, J. Pan, F. Adamietz, V. Rodriguez, L. Ducasse, F. Castet, A. Plaquet and B. Champagne, Two-Way Molecular Switches with Large Nonlinear Optical Contrast, *Chem. – Eur. J.*, 2009, **15**, 2560–2571.
83 A. Plaquet, B. Champagne, J. Kulhánek, F. Bureš, E. Bogdan, F. Castet, L. Ducasse and V. Rodriguez, Effects of the Nature and Length of the π-Conjugated Bridge on the Second-Order Nonlinear Optical Responses of Push–Pull Molecules Including 4,5-Dicyanoimidazole and Their Protonated Forms, *ChemPhysChem*, 2011, **12**, 3245–3252.

